

Source-Free Domain Adaptation for Geospatial Point Cloud Semantic Segmentation

Yuan Gao^{a,b,c}, Di Cao^e, Xiaohuan Xi^{a,b,c}, Sheng Nie^{a,b,c}, Shaobo Xia^{d,*}, Cheng Wang^{a,b,c}

^a*Aerospace Information Research Institute, Chinese Academy of Sciences, Beijing 100094, China*

^b*International Research Center of Big Data for Sustainable Development Goals, Beijing 100094, China*

^c*University of Chinese Academy of Sciences, Beijing 100094, China*

^d*School of Aeronautic Engineering, Changsha University of Science and Technology, Changsha 410004, China*

^e*Zhengzhou Institute for Advanced Research of Henan Polytechnic University, Henan Polytechnic University, Zhengzhou 451464, China*

Abstract

Semantic segmentation of 3D geospatial point clouds is pivotal for remote sensing applications. However, variations in geographic patterns across regions and data acquisition strategies induce significant domain shifts, severely degrading the performance of deployed models. Existing domain adaptation methods typically rely on access to source-domain data. However, this requirement is rarely met due to data privacy concerns, regulatory policies, and data transmission limitations. This motivates the largely underexplored setting of source-free unsupervised domain adaptation (SFUDA), where only a pretrained model and unlabeled target-domain data are available. In this paper, we propose LoGo (Local–Global Dual-Consensus), a novel SFUDA framework specifically designed for geospatial point clouds. At the local level, we introduce a class-balanced prototype estimation module that abandons conventional global threshold filtering in favor of an intra-class independent anchor mining strategy. This ensures that robust feature prototypes can be generated even for sample-scarce tail classes, effectively mitigating the feature collapse caused by long-tailed distributions. At the global level, we introduce an optimal transport-based global distribution alignment module that formulates pseudo-label assignment as a global optimization problem. By enforcing global distribution constraints, this module effectively corrects the over-dominance of head classes inherent in local greedy assignments, preventing model predictions from being severely biased towards majority classes. Finally, we propose a dual-consistency pseudo-label filtering mechanism. This strategy retains only high-confidence pseudo-labels where local multi-augmented ensemble predictions align with global optimal transport assignments for self-training. Extensive experiments on two challenging benchmarks, encompassing cross-scene and cross-sensor settings, demonstrate that LoGo consistently outperforms existing state-of-the-art methods. Notably, LoGo achieves mIoU improvements of 5.9% on the STPLS3D → H3D task and 11.42% on the DALES → T3D task compared to the source-only baseline. The source code is available at <https://github.com/GYproject/LoGo-SFUDA>.

Keywords: Point cloud, Semantic segmentation, Source-free unsupervised domain adaptation, Optimal Transport

1. Introduction

3D geospatial point clouds—acquired via Airborne Laser Scanning (ALS), Mobile Laser Scanning (MLS), and photogrammetry—provide precise geometric representations of the real world. They form the foundation for cadastral surveying [1], land cover mapping [2], and 3D reconstruction [3], making semantic segmentation of large-scale 3D urban scenes a critical research topic. While deep learning-based methods (e.g., PointNet++ [4], KPConv [5]) have demonstrated remarkable capabilities. However, in practical large-scale geospatial scenarios, variations in sensor modalities and data acquisition mechanisms introduce considerable domain shift, leading to performance degradation when models trained on source domains are applied to unseen target scenes, as shown in Fig. 1 a. This phenomenon, commonly referred to as domain shift, primarily stems from two distinct factors in geospatial data: cross-scene variations and cross-sensor discrepancies. On one hand,

cross-scene shift arises from the intrinsic diversity of urban environments. Differences in architectural styles, city layouts, and vegetation types across geographically distinct regions result in significant distributional discrepancies in class definitions and object appearances. On the other hand, cross-sensor shift is introduced by distinct data acquisition mechanisms. For instance, ALS typically captures bird’s-eye views with relatively sparse density and uniform distribution, whereas MLS provides dense, street-level details but suffers from severe occlusions. Furthermore, photogrammetry-derived data exhibits a fundamental structural disparity compared to active LiDAR. While LiDAR captures volumetric information by penetrating vegetation gaps, photogrammetry is inherently limited to surface-level geometry inferred from multi-view matching, often resulting in distinct noise distributions and a lack of sub-canopy details. Such variations in point density, geometric structure, and viewing angles create a substantial feature gap between domains, hindering the generalization capability of deep learning models.

Unsupervised Domain Adaptation (UDA) has emerged as the mainstream paradigm to address this shift [6]. As shown in

*Corresponding author.

Email address: shaoboxia2020@gmail.com (Shaobo Xia)

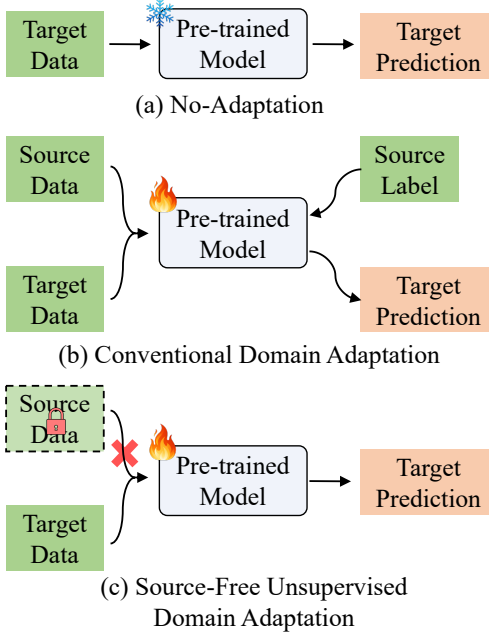


Figure 1: Overview of domain adaptation paradigms. ■ Model Input, ■ Model Output. The snowflake indicates frozen parameters, while the flame indicates trainable parameters. (a) No Adaptation; (b) Conventional Domain Adaptation; (c) Source-Free Unsupervised Domain Adaptation.

Fig. 1 b, traditional UDA methods typically assume concurrent access to labeled source data and unlabeled target data. By employing strategies such as adversarial learning and feature alignment, UDA explicitly reduces the distribution discrepancy between the source and target domains in the feature space, thereby successfully transferring discriminative knowledge from the source to the target. This paradigm effectively circumvents the reliance on laborious target domain annotations, offering a cost-effective and scalable solution for large-scale geospatial applications. However, the assumption of "concurrent access to source and target data" often fails in practical surveying and remote sensing deployments. Geospatial data frequently involves national security or commercial sensitivity, where data sharing is constrained by strict privacy regulations. Consequently, end-users are often restricted to accessing only pre-trained model, without access to the source data. Facing the dual challenges of "domain shift" and "inaccessible source data," Source-Free Domain Adaptation (SFUDA) has become a promising direction to achieve high-precision semantic segmentation, as shown in Fig. 1 c. SFUDA aims to perform adaptation utilizing only the pre-trained source model and unlabeled target data, effectively alleviating domain shift while strictly adhering to data privacy.

While SFUDA shows promise, existing research in the 3D point cloud domain predominantly focuses on autonomous driving [7]. Such studies typically address minor shifts between homogeneous sensors (e.g., LiDARs with different beam counts) and implicitly assume minimal viewpoint variation. However, directly applying these methods to geospatial scenarios faces two major obstacles. First, cross-modality and view-

point discrepancies are significant. Geospatial data is highly heterogeneous; transferring from photogrammetry (surface-only) to ALS (volumetric) involves fundamental structural differences. Similarly, shifting from airborne (nadir view) to mobile (ground view) systems renders many geometric priors ineffective. Second, class imbalance is more severe in geospatial scenes. Unlike street scenes, geospatial environments are heavily dominated by background elements. For instance, in the DALES benchmark [8], ground and vegetation account for approximately 80.89% of the total points. In contrast, critical objects like fences and power lines are extremely sparse, constituting merely 0.52% and 0.20%, respectively. This long-tailed distribution causes conventional methods to neglect tail classes, leading to missed detections. However, SFUDA for heterogeneous geospatial point clouds remains largely unexplored.

To bridge this gap, we propose a novel SFUDA framework named LoGo (Local-Global Dual-Consensus). Specifically, we adopt a parameter-efficient fine-tuning strategy by freezing the pre-trained classifier and feature extractor while optimizing only the Batch Normalization (BN) layers, which effectively adapts to target statistics while preserving the source domain's learned geometric structure. To generate high-precision pseudo-labels, our approach integrates a Class-Balanced Local Prototype Estimation module. By adopting an Intra-class Anchor Mining strategy, we construct robust prototypes based on high-confidence anchors within each category, effectively mitigating class imbalance. Building on this, we incorporate global constraints via global distribution alignment using Optimal Transport (OT), where the Sinkhorn algorithm aligns samples based on global class priors to rectify the bias inherent in local greedy assignments. Finally, to ensure training stability under domain shift, we employ Local-Global Dual-Consensus Filtering, which selects only those pseudo-labels where the model's local ensemble predictions reach a consensus with the global OT assignments, thereby effectively suppressing noise propagation.

Our main contributions are summarized as follows:

- To the best of our knowledge, this work represents the first attempt to investigate the cross-scene and cross-sensor geospatial point cloud segmentation task (e.g., Photogrammetry \rightarrow LiDAR) under the strict SFUDA setting. We specifically address the challenges of privacy constraints and significant domain shift without accessing source data.
- We propose LoGo, a robust self-training framework that synergizes Class-Balanced Local Prototype Estimation with Global Distribution Alignment via Optimal Transport. By enforcing a Dual-Consensus between local feature patterns and global distributional constraints, our method effectively rectifies the bias induced by long-tailed distributions and suppresses pseudo-label noise.
- Extensive experiments on two challenging benchmarks (covering Photogrammetry, ALS, and MLS data) demonstrate that our method achieves state-of-the-art performance. The results validate that our LoGo framework effectively bridges cross-scene and cross-sensor gaps, offer-

ing a practical and privacy-preserving solution for large-scale geospatial mapping.

The remainder of this article is organized as follows. Section 2 reviews related studies in point cloud semantic segmentation, domain adaptation for point clouds, and source-free unsupervised domain adaptation. Section 3 details the proposed LoGo framework. Subsequently, Section 4 presents comparative experiments and ablation studies. Finally, Section 5 concludes the paper and discusses future research directions.

2. Related Work

2.1. Semantic Segmentation of 3D Point Clouds

3D point cloud semantic segmentation aims to assign semantic labels to every point within unordered point clouds, serving as a fundamental task for 3D scene understanding. With the advancement of deep learning techniques, existing fully supervised segmentation paradigms generally fall into three categories: projection-based, voxel-based, and point-based methods.

Early explorations mainly attempted to leverage mature 2D Convolutional Neural Networks (CNNs). These projection-based methods [9, 10] map 3D point clouds into 2D images to reuse standard CNN architectures; however, this projection process inevitably results in geometric information loss. To directly preserve the 3D geometric structure, voxel-based methods were proposed. Sparse Convolution techniques [11, 12] significantly reduce computational complexity by performing operations exclusively on non-empty voxels.

Point-based methods operate directly on unstructured point clouds to extract features. As a pioneering work, PointNet++ [4] extracts local features through hierarchical sampling and multi-scale grouping. To better capture local geometric topology, DGCNN [13] employs dynamic graph convolution (Edge-Conv) to construct neighborhood relations in the feature space. Addressing efficient inference for large-scale scenes, RandLA-Net [14] introduces a random sampling strategy and a local feature aggregation module, significantly reducing memory consumption. KPConv [5] achieves high-quality continuous space convolution by defining deformable Kernel Points. Due to its robustness to varying point densities and capability in preserving fine-grained local geometric details, KPConv has become a preferred backbone for complex outdoor scene parsing. Recently, Transformer-based architectures [15, 16] have also emerged, demonstrating superior performance by modeling long-range dependencies, though often at a higher computational cost.

Although the aforementioned fully supervised methods achieve significant progress on standard benchmarks, they depend heavily on massive and high-quality point-wise annotations, which are laborious and expensive to acquire for 3D data. More critically, existing models typically assume training and testing data share identical statistical characteristics. In real-world applications, models face domain shift due to heterogeneous sensors or environmental changes, leading to noticeable

performance degradation on unlabeled target scenes. This dependence on annotated data and the lack of cross-domain robustness render research on UDA imperative.

2.2. Domain Adaptation for Point clouds

To mitigate performance degradation in cross-domain scenarios, UDA aims to align the data distribution of the unlabeled target domain with the source domain. Existing point cloud UDA methods primarily follow two mainstream approaches: adversarial feature alignment and self-training.

Adversarial training attempts to learn domain-invariant representations by minimizing the feature space distance between domains [17, 18, 19, 20, 21]. ePointDA [17] proposes a self-supervised strategy simulating real-world degradation via Dropout noise on synthetic data. It combines statistics-invariant Instance Normalization with spatially adaptive convolution for feature alignment, thereby enhancing cross-domain segmentation performance without relying on real-domain statistical priors. Addressing differences in sensor characteristics, Li et al. [20] observe that domain shift largely stems from the structural differences between complete synthetic point clouds and real LiDAR data, which contain irregular noise such as missing points. They employ an adversarial training mechanism to guide a Masking Module, which simulates real noise distributions, effectively reducing domain discrepancy through feature alignment.

Self-training strategies focus on iterative optimization using target domain pseudo-labels [22, 23, 24, 25]. To preserve spatial semantic continuity, ConDA [22] leverages the spatial structure of Range View (RV) images by constructing an intermediate domain through non-overlapping splicing of source and target image strips. This approach facilitates inter-domain interaction while maintaining semantic coherence around autonomous vehicles; additionally, an entropy aggregator filters high-confidence pseudo-labels. LiDAR-UDA [25] focuses on mitigating domain shift caused by sensor configuration differences, particularly beam density and scanning patterns. This method employs structured point cloud downsampling to simulate diverse scan patterns, enhancing robustness to sparse data. Furthermore, by exploiting the temporal consistency of point cloud sequences to perform weighted fusion of multi-frame predictions, it generates high-quality refined pseudo-labels to guide self-training in the target domain.

To address complex cross-scene and cross-sensor challenges in geospatial point clouds, several studies propose targeted solutions. To address domain shift in urban MLS caused by varying urban morphologies (e.g., building height), Luo et al. [6] design a Point-wise Attention Transformation Module (PW-ATM) to align vertical height distributions in the input space; subsequently, combined with Maximum Classifier Discrepancy (MCD), it aligns feature distributions in the latent space. Additionally, Luo et al. [26] utilize Approximate Unsigned Distance Fields to reconstruct continuous latent scene surfaces, mapping both source and target point clouds into a unified Canonical Domain.

Although effective, these UDA methods assume concurrent access to source and target data. In practical surveying and re-

mote sensing applications, accessing raw source data is often restricted by privacy policies, transmission bandwidth, and storage costs. These constraints necessitate a shift towards Source-Free Domain Adaptation (SFUDA).

2.3. Source-Free Unsupervised Domain Adaptation

SFUDA addresses the domain shift problem using only a pre-trained source model, without access to source data. Initially explored in the 2D image domain, this paradigm includes generative methods, fine-tuning-based methods, and self-training methods.

Generative methods [27, 28, 29] synthesize pseudo-samples using Generative Adversarial Networks (GANs) or source model statistics to assist alignment [30, 31], though often with high computational overhead. Fine-tuning-based methods focus on immediate inference-time adaptation; for instance, Tent [32] and DUA [33] minimize prediction entropy or update Batch Normalization (BN) statistics online. In contrast, pseudo-label-based self-training methods [34, 35, 36, 37] typically adopt an offline iterative mode. SHOT [38] freezes the classifier and maximizes information flow, employing a global prototype-based strategy to align target features with the source hypothesis. C-SFDA [37] further introduces a dynamic selection mechanism based on prediction confidence, adhering to an “easy-to-hard” curriculum to suppress error accumulation.

Recently, SFUDA has been extended to the 3D point cloud domain, primarily focusing on autonomous driving. Michele et al. [7] propose a framework utilizing source class distribution priors and consistency with a reference model as unsupervised stopping criteria, achieving stable fine-tuning. TGSF [39] employs a Bi-directional Pseudo-Label Selection (BPLS), dynamically distinguishing between source-similar and source-distinct data based on entropy to extract reliable pseudo-labels, while leveraging a teacher-student architecture to enforce global and class prototype consistency to prevent model collapse. Beyond segmentation, SFUDA has also been investigated in 3D object detection [40, 41, 42], point cloud completion [43, 44], and primitive segmentation [45, 46].

For geospatial point clouds, research is still in its early stages. Liu et al. [47] target urban-scale point cloud segmentation by projecting 3D point clouds into 2D Bird’s-Eye-View (BEV) images. They employ geometric priors (normal vectors, height) to correct geometric information lost during projection, leveraging 2D foundation models to generate high-quality pseudo-labels to guide 3D network training. Addressing test-time adaptation, Wang et al. [48] design a progressive BN update strategy guided by reliability-constrained pseudo-labels.

However, existing methods exhibit limitations in complex heterogeneous sensor transfer. For instance, Liu et al. [?] rely on 2D foundation models via BEV projection, which may struggle to fully capture fine-grained vertical geometric details, limiting performance on overlapping structures like overpasses. Furthermore, their geometric correction strategy based on fixed thresholds lacks adaptability in complex terrains. Conversely, while targeting 3D data directly, the TTA paradigm of Wang et al. [48] is constrained by the limited receptive field of online inference. In geospatial scenes with strong spatial heterogeneity,

extreme class skew within local batches (e.g., vegetation-only batches) causes fluctuations in BN statistics, compromising the global semantic consistency essential for large-scale mapping. To address these challenges, we propose a purely 3D offline adaptation framework. Unlike projection-based methods, we preserve complete 3D geometric information. Furthermore, to overcome the instability of batch-wise adaptation, we introduce a global optimization strategy based on Optimal Transport, ensuring robust distribution alignment even under severe class imbalance.

3. Methodology

To mitigate domain distribution shift and the lack of supervision in the SFUDA setting, we propose a robust self-training framework, termed LoGo (Local-Global Dual-Consensus). The overall pipeline is illustrated in Fig. 2. We adopt an iterative “Offline Self-Training” paradigm. Built upon a parameter-efficient Mean-Teacher paradigm, our approach refines pseudo-labels through three core modules. First, to reduce prediction uncertainty, we employ a Multi-Augmented Ensemble strategy. Subsequently, the Class-Balanced Local Prototype Estimation (CBLPE) module constructs reliable feature prototypes from a local intra-class perspective. Following this, the Global Distribution Alignment (GDA) module leverages Optimal Transport to enforce global distributional constraints and regularize class assignments. Ultimately, the Local-Global Dual-Consensus Filtering (LGDCF) module integrates these distinct views to curate reliable pseudo-labels for student model supervision.

3.1. Problem Formulation and Framework

3.1.1. Source-Free Unsupervised Domain Adaptation Setting

We formulate the SFUDA task within the context of 3D point cloud semantic segmentation. Formally, let \mathcal{X} denote the input space comprising point coordinates and features, and $\mathcal{Y} = \{1, \dots, K\}$ represent the shared discrete label space. The segmentation network is decomposed into a feature encoder $G : \mathcal{X} \rightarrow \mathcal{F}$, which maps inputs to a high-dimensional feature space $\mathcal{F} \subseteq \mathbb{R}^D$, and a classifier $C : \mathcal{F} \rightarrow \mathbb{R}^K$, which projects features to class logits.

We consider a source domain \mathcal{D}_S and an unlabeled target domain $\mathcal{D}_T = \{x_i\}_{i=1}^N$, where N denotes the total number of target points. Crucially, we operate under the Closed-Set assumption ($\mathcal{Y}_S = \mathcal{Y}_T$), tackling the challenge where feature distributions differ significantly ($\mathcal{P}_S(x) \neq \mathcal{P}_T(x)$).

The SFUDA protocol proceeds in two stages: first, the source model $M_S = C \circ G$ is pre-trained on \mathcal{D}_S via standard supervision; subsequently, in the adaptation phase, access to \mathcal{D}_S is restricted. Our objective is to adapt the model parameters—initialized with pre-trained weights θ_S —to align the target representation utilizing only the unlabeled target data \mathcal{D}_T .

3.1.2. Parameter-Efficient Mean-Teacher Architecture

To achieve robust adaptation under unsupervised conditions, we adopt a self-training framework based on the Mean-Teacher paradigm [49]. This framework comprises a student model

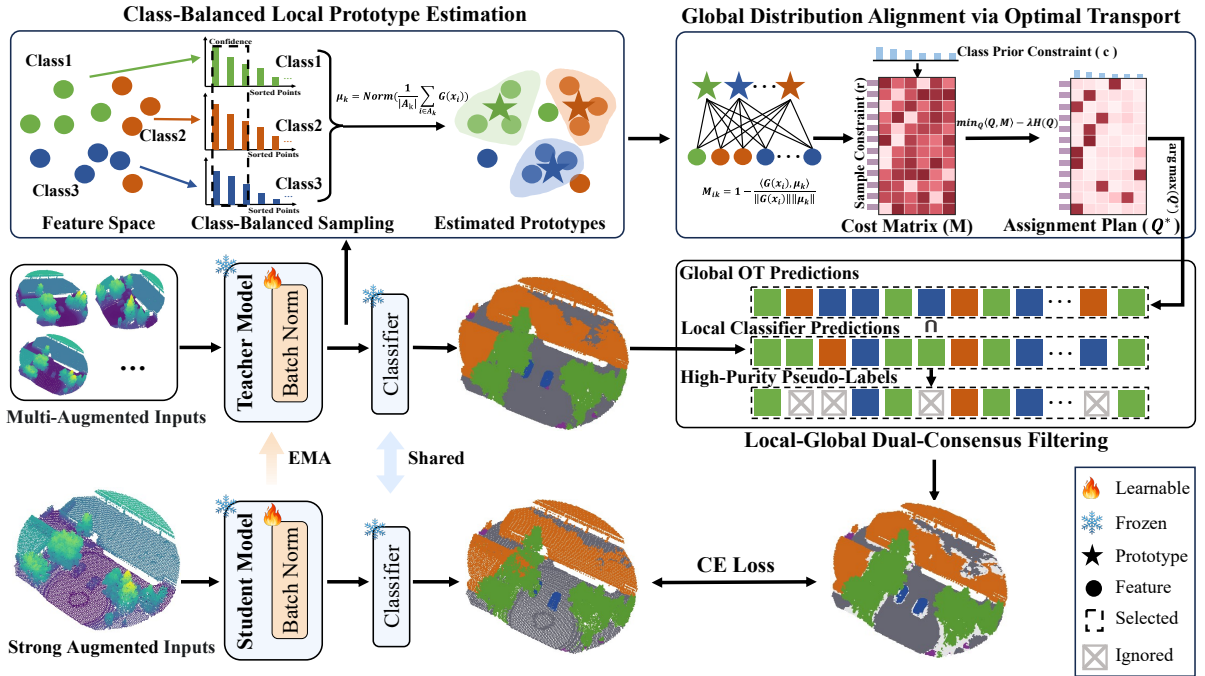


Figure 2: Overview of the proposed LoGo framework. The architecture adheres to a parameter-efficient Mean-Teacher paradigm, where only the BN layers are learnable (indicated by the flame icon), while other parameters remain frozen (snowflake icon). The adaptation process begins by aggregating features from multi-augmented inputs via the **Class-Balanced Local Prototype Estimation (CBLPE)** module, which employs an intra-class anchor mining strategy to estimate robust class prototypes. Subsequently, the **Global Distribution Alignment (GDA)** module solves an Optimal Transport problem to generate a global assignment plan \mathbf{Q}^* by minimizing transport costs under class prior constraints. Finally, the **Local-Global Dual-Consensus Filtering (LGDCF)** mechanism selects reliable pseudo-labels by identifying the intersection (\cap) between local classifier predictions and global OT assignments. The student model is then supervised by these refined labels on strongly augmented data via Cross-Entropy (CE) loss, while the teacher model evolves through Exponential Moving Average (EMA).

M_{stu} , updated via gradient descent, and a teacher model M_{tea} , evolved via Exponential Moving Average (EMA), as shown in Fig. 2. Since full fine-tuning risks overfitting to noisy pseudo-labels and distorting the pre-trained feature space, we adopt a parameter-efficient strategy [38]. Specifically, we freeze the convolutional weights of the feature extractor G and the parameters of the classification head C , optimizing only the affine parameters of the Batch Normalization (BN) layers. This strategy enables the model to rapidly align with the target domain distribution by recalibrating feature statistics while preserving the discriminative power of the pre-trained representations.

3.2. Class-Balanced Local Prototype Estimation

Prior to each training epoch, we perform a global inference pass to update pseudo-labels. In the absence of source supervision, feature alignment relies heavily on constructing reliable class prototypes. A naive approach aggregates features based directly on raw predictions. However, in geospatial point clouds characterized by severe domain shifts and long-tailed distributions, such uniform aggregation is risky. It often leads to "representation collapse," where tail-class prototypes are overwhelmed by misclassified samples from head classes due to prediction bias.

To address this challenge, we propose the Class-Balanced Local Prototype Estimation (CBLPE) module, as shown in Fig. 2. Conventional methods typically rely on a global confidence

threshold, which inadvertently filters out tail classes that naturally have lower confidence. In contrast, our module adopts a class-aware "local selection" strategy. By independently mining high-confidence anchors within each category, CBLPE ensures that even under-represented classes maintain robust and distinct prototypes. This effectively prevents noise accumulation from dominant classes.

3.2.1. Multi-Augmented Ensemble Inference

To suppress prediction variance caused by point cloud sparsity, we introduce a multi-augmented ensemble mechanism. At each epoch, the teacher model M_{tea} processes the entire dataset \mathcal{D}_T under V augmentation transformations (e.g., rotation). We aggregate the predictions to obtain a smoothed probability distribution $\bar{\mathbf{p}}_i$:

$$\bar{\mathbf{p}}_i = \frac{1}{V} \sum_{v=1}^V \sigma(C_{tea}(G_{tea}(\mathcal{T}_v(x_i)))) \quad (1)$$

where $\mathcal{T}_v(\cdot)$ denotes the v -th random transformation, and σ is the Softmax function. This process yields probability estimates that are more robust against input noise.

3.2.2. Local Confidence Metric

Based on the smoothed probability distribution, we extract the raw prediction label $\hat{y}_{raw,i}$ and confidence score s_i for each sample:

$$\hat{y}_{raw,i} = \arg \max(\bar{\mathbf{p}}_i), \quad s_i = \max(\bar{\mathbf{p}}_i) \quad (2)$$

where s_i quantifies the model’s certainty regarding the sample assignment.

3.2.3. Intra-class Anchor Mining

Traditional pseudo-label filtering strategies often rely on a global unified confidence threshold (e.g., $\delta = 0.9$). However, under severe class imbalance, the prediction confidence for tail classes is consistently low. Consequently, these classes are prone to being filtered out, leading to a bias towards majority classes.

To address this, we propose an intra-class independent mining strategy that performs filtering separately within each category. For any class $k \in \{1, \dots, K\}$, we construct a candidate set $\mathcal{I}_k = \{i \in \{1, \dots, N\} \mid \hat{y}_{raw,i} = k\}$. Instead of a fixed threshold, we select the top ρ percentage of samples (e.g., $\rho = 0.8$) to form the high-confidence anchor set \mathcal{A}_k :

$$\mathcal{A}_k = \{i \in \mathcal{I}_k \mid \text{rank}_{\mathcal{I}_k}(s_i) \leq \lfloor \rho \cdot |\mathcal{I}_k| \rfloor\} \quad (3)$$

where $\text{rank}_{\mathcal{I}_k}(s_i)$ denotes the ranking index of sample i within the global candidate set \mathcal{I}_k sorted by confidence in descending order. This design follows the principle of relative reliability: it ensures that even for difficult tail classes, the most reliable subset is utilized to represent the class distribution.

3.2.4. Feature Prototype Aggregation

Based on the anchor set \mathcal{A}_k , the prototype μ_k for category k is calculated as the normalized mean of the features of the samples in the set:

$$\mu_k = \text{Normalize} \left(\frac{1}{|\mathcal{A}_k|} \sum_{i \in \mathcal{A}_k} G_{fea}(x_i) \right) \quad (4)$$

These prototypes serve as geometric centroids within the target feature space, representing the unique local structural characteristics of each category.

3.3. Global Distribution Alignment via Optimal Transport

With the constructed class-balanced prototypes μ_k , a standard approach to generate pseudo-labels is greedy assignment, which assigns each sample to its nearest prototype based on feature similarity. However, this sample-wise independent strategy is highly vulnerable to feature bias caused by domain shift. It often over-assigns ambiguous samples to majority classes, resulting in severely biased pseudo-labels.

To overcome this limitation, we introduce the Global Distribution Alignment (GDA) module, which formulates pseudo-label generation as an Optimal Transport (OT) problem [50], as shown in Fig. 2. Unlike greedy assignment which optimizes locally, OT treats the assignment process as a global distribution alignment problem. It seeks a globally optimal alignment plan that minimizes the total transport cost while strictly enforcing specific marginal distribution constraints. Crucially, this mechanism prevents majority classes from over-claiming ambiguous samples, ensuring that valid samples for minority classes are preserved.

3.3.1. Global Cost Matrix Construction

We formulate pseudo-label assignment as a minimum-cost transport problem between the sample feature set and the category prototype set. First, we construct a global affinity cost matrix $\mathbf{M} \in \mathbb{R}^{N \times K}$, where the element M_{ik} measures the cosine distance between the i -th sample and the k -th prototype in the feature space:

$$M_{ik} = 1 - \frac{\langle G(x_i), \mu_k \rangle}{\|G(x_i)\| \|\mu_k\|} \quad (5)$$

This matrix quantifies the geometric cost of assigning samples to respective categories.

3.3.2. Entropy-Regularized Sinkhorn Optimization

To achieve global distribution alignment, we solve for an optimal assignment matrix \mathbf{Q}^* , aiming to minimize the total transport cost while satisfying specific marginal distribution constraints. The optimization objective is defined as:

$$\mathbf{Q}^* = \arg \min_{\mathbf{Q} \in \mathbb{U}(\mathbf{r}, \mathbf{c})} \sum_{i=1}^N \sum_{k=1}^K Q_{ik} M_{ik} - \lambda H(\mathbf{Q}) \quad (6)$$

where λ is the regularization coefficient, and $H(\mathbf{Q})$ is the entropy regularization term. The constraint set $\mathbb{U}(\mathbf{r}, \mathbf{c})$ formalizes the global prior:

$$\mathbb{U}(\mathbf{r}, \mathbf{c}) = \{\mathbf{Q} \in \mathbb{R}_+^{N \times K} \mid \mathbf{Q} \mathbf{1}_K = \mathbf{r}, \mathbf{Q}^\top \mathbf{1}_N = \mathbf{c}\} \quad (7)$$

Here, $\mathbf{r} = \frac{1}{N} \mathbf{1}_N$ enforces that every sample is assigned equal weight. The vector $\mathbf{c} \in \mathbb{R}^K$ represents the global target class prior. In our offline setting, we assume that while individual predictions may contain noise, the aggregate statistics provide a stable estimate of the domain’s class distribution. Thus, \mathbf{c} is calculated from the global statistics of the ensemble predictions: $c_k = \frac{|\mathcal{I}_k|}{\sum_j |\mathcal{I}_j|}$. This transforms local statistical information into boundary conditions for global optimization.

We utilize the Sinkhorn-Knopp algorithm [51] to efficiently solve this convex optimization problem iteratively, ultimately obtaining the optimal assignment labels $\hat{y}_{sink,i} = \arg \max_k Q_{ik}^*$ from a global perspective. The Sinkhorn algorithm enforces an inter-class competition mechanism, compelling the model to seek an optimal solution that conforms to global class distribution.

3.4. Local-Global Dual-Consensus Filtering

Even with robust prototypes and global alignment, individual pseudo-labels may still carry noise due to the inherent conflict between local feature similarity and global distributional constraints. Relying exclusively on either view can lead to biased supervision. To resolve this ambiguity, we propose the Local-Global Dual-Consensus Filtering (LGDCF) strategy, as shown in Fig. 2. The core insight is to exploit the complementarity of the two views: we identify the intersection between the multi-augmented ensemble prediction (Local View) and the Sinkhorn optimization assignment (Global View), retaining only those samples where feature-based confidence aligns with global distributional optimality. The final pseudo-label $\hat{y}_{final,i}$ is generated as:

$$\hat{y}_{final,i} = \begin{cases} \hat{y}_{raw,i}, & \text{if } \hat{y}_{raw,i} = \hat{y}_{sink,i} \\ \text{ignore}, & \text{otherwise} \end{cases} \quad (8)$$

This mechanism ensures reliability: When $\hat{y}_{raw} = \hat{y}_{sink}$, the sample is not only highly matched with a specific prototype in terms of local features but is also assigned to the same category after verification through global distribution constraints and inter-class competition. Such samples are regarded as reliable pseudo-labels. When the two are inconsistent, the sample likely resides in an overlapping region of the feature space or on a decision boundary. The local view may misjudge due to minor feature perturbations, while the global view may enforce a bias correction that contradicts local semantics. For such samples with semantic ambiguity, we flag them as ignore and exclude them from gradient backpropagation.

3.5. Optimization and Temporal Ensembling

Following the offline pseudo-label generation phase, we proceed to the parameter optimization stage. In this stage, the generated global pseudo-labels \hat{y}_{final} are assigned to the target dataset \mathcal{D}_T . We then construct a data loader to iterate over \mathcal{D}_T in mini-batches for standard supervised learning.

The student model M_{stu} is trained by minimizing the Cross-Entropy loss on the filtered valid samples:

$$\mathcal{L}_{ce} = -\frac{1}{|\mathcal{B}_{valid}|} \sum_{x_i \in \mathcal{B}_{valid}} \log P(y = \hat{y}_{final,i} | x_i; \theta_{stu}) \quad (9)$$

where $\mathcal{B}_{valid} = \{x_i \in \mathcal{B} \mid \hat{y}_{final,i} \neq \text{ignore}\}$ denotes the set of valid samples within the current mini-batch \mathcal{B} . By utilizing these high-quality pseudo-labels derived from the global consensus, the student model is guided to learn robust decision boundaries.

To further enhance the stability of the training process, the teacher model M_{tea} does not participate in gradient descent but evolves through temporal ensembling of the student model parameters. Specifically, at each training step t , the teacher parameters θ_{tea} are updated as follows:

$$\theta_{tea}^{(t)} = \alpha \theta_{tea}^{(t-1)} + (1 - \alpha) \theta_{stu}^{(t)} \quad (10)$$

where α is the momentum coefficient (set to 0.999 in our experiments). This EMA mechanism effectively smooths the optimization trajectory. Crucially, since the teacher model is used to generate pseudo-labels for the next epoch, this temporal smoothing ensures that the generated supervision signals remain stable and do not oscillate drastically between epochs, thereby preventing error amplification.

4. Experiments

4.1. Dataset and Benchmark

4.1.1. Dataset Description

STPLS3D [52] is a large-scale aerial photogrammetry point cloud dataset containing real-world and synthetic urban scenes

covering a total area of over 17 km². The real-world subset covers approximately 1.27 km², reconstructed using photogrammetry techniques from high-overlap aerial images collected via Unmanned Aerial Vehicles (UAVs) across four distinct regions, including the University of Southern California (USC). The synthetic subset covers approximately 16 km² (62 scenes) and is generated from geospatial data (e.g., OSM) through a procedural pipeline simulating real UAV flight paths and reconstruction processes. It features typical Bird's-eye View (BEV) geometry and RGB attributes. The synthetic portion provides 18 categories, including Building, Low Vegetation, Medium Vegetation, High Vegetation, Car, Truck, Aircraft, Military Vehicle, Bike, Motorcycle, Light Pole, Street Sign, Clutter, Fence, Road, Window, Dirt, and Grass.

H3D (Hessigheim 3D) [53] is a high-resolution UAV LiDAR benchmark dataset acquired in Hessigheim, Germany. Collected by a RIEGL VUX-1LR laser scanner at a 50 m altitude, it features an average density of 800 pts/m². The labeled data for experiments (including training and validation sets) comprises approximately 159 million points. Each point contains spatial coordinates (X, Y, Z), reflectance, echo number, and RGB color attributes obtained via photogrammetric mesh mapping. The dataset is annotated with 11 categories: Low Vegetation, Impervious Surface, Vehicle, Urban Furniture, Roof, Facade, Shrub, Tree, Soil/Gravel, Vertical Surface, and Chimney.

DALES (Dayton Annotated LiDAR Earth Scan) [8] is a large-scale Airborne Laser Scanning (ALS) point cloud dataset acquired over Surrey, British Columbia, Canada. It covers an area of 10 km² and contains over 505 million points, collected by a Riegl Q1560 dual-channel airborne LiDAR system at a flight altitude of approximately 1300 m, with an average point density of about 50 pts/m². Each point includes spatial coordinates (X, Y, Z), intensity, and return number attributes. The dataset contains 8 semantic class labels: Ground, Vegetation, Building, Vehicle, Truck, Power Line, Pole, and Fence.

T3D (Toronto-3D) [54] is an urban outdoor scene dataset collected via a vehicle-based Mobile Laser Scanning (MLS) system. It was acquired on Avenue Road in Toronto, Canada, covering a road segment of approximately 1 km and containing about 78.3 million points. It was captured by a Teledyne Optech Maverick mobile mapping system equipped with a 32-line LiDAR sensor, featuring a point density of approximately 1000 pts/m² on road surfaces. Attributes include spatial coordinates (X, Y, Z), RGB color, intensity, GPS time, and scan angle. It is annotated with 8 categories, including: Road, Road Marking, Natural, Building, Utility Line, Pole, Car, and Fence.

4.1.2. Benchmark

To evaluate our method in geospatial applications, we designed two transfer protocols addressing key domain shifts in urban mapping:

Task 1: STPLS3D → H3D. This setting simulates a practical "Low-Cost to High-Precision" transfer scenario, characterized by severe discrepancies in sensor modality and scene layout. The primary challenge stems from the fundamental structural gap between photogrammetry and LiDAR. The source data (STPLS3D), derived from passive aerial imagery, is prone

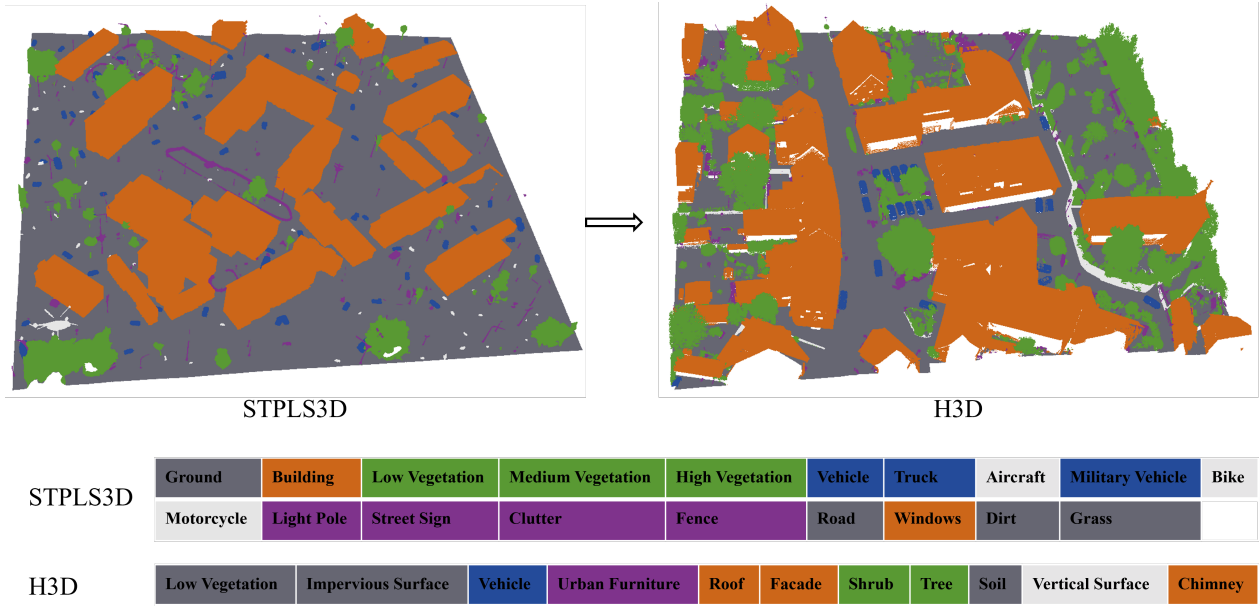


Figure 3: **Visualization of the domain adaptation scenario from photogrammetry-derived point clouds (STPLS3D) to UAV-based LiDAR point clouds (H3D).** The top row compares the representative scenes, while the bottom row displays their corresponding semantic label spaces.

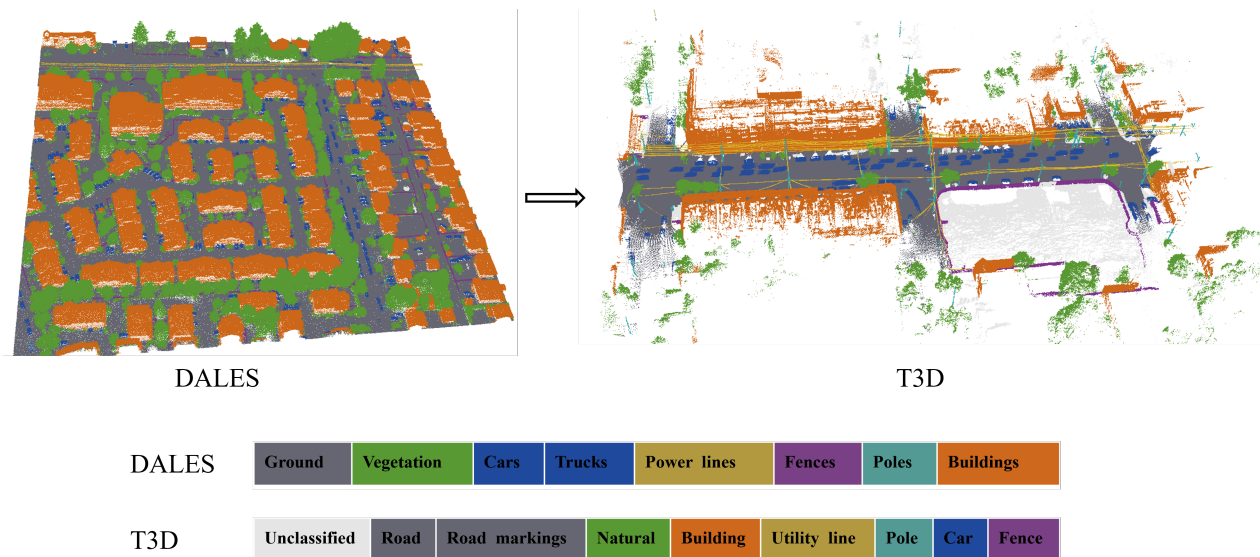


Figure 4: **Visualization of the domain adaptation scenario from ALS point clouds (DALES) to MLS point clouds (T3D).** The top row compares the representative scenes, while the bottom row displays their corresponding semantic label spaces.

to geometric noise and blurred structural boundaries, and critically, it lacks vegetation penetration capability, resulting in surface-only representations. In contrast, the target data (H3D) consists of precise, high-resolution UAV LiDAR scans (800 pts/m²) with sharp geometry and intensity attributes. This cross-sensor shift is further compounded by the scene divergence: transferring from synthetic environments generated by procedural pipelines to real-world German villages introduces significant discrepancies in architectural styles and object textures. We define 5 common categories for alignment: *Ground*, *Vehicle*, *Urban Furniture*, *Building*, and *Vegetation* (Fig. 3).

Task 2: DALES → T3D.

This setting addresses the drastic "Nadir-View to Street-View" shift, introducing extreme geometric and density variations driven by distinct acquisition mechanisms. The domain gap is profound: the source data (DALES) is collected via Airborne Laser Scanning (ALS) from a high altitude of 1300 m, resulting in sparse point clouds (50 pts/m²) that predominantly capture rooftops and large-scale terrain. Conversely, the target data (Toronto-3D) is acquired by Mobile Laser Scanning (MLS) along a single road segment, offering dense street-level details (1000 pts/m²) but missing building tops. Furthermore, the scene context shifts from wide-area aerial surveys to focused urban street corridors. The model must essentially learn to infer detailed street-level semantics from sparse top-down priors. We define 5 common categories for alignment: *Ground*, *Vehicle*, *Urban Furniture*, *Building*, and *Vegetation* (Fig. 3).

4.2. Implementation Details

All models are implemented in PyTorch 1.8.2 on a single NVIDIA GeForce GTX 3090 24GB GPU. We adopt KP-Conv (KPFNN) [5] as the 3D backbone, following the default configuration of the official open-source repository. We rely solely on 3D coordinates to ensure the method's generalizability across sensors with diverse attribute configurations. To accommodate the density and scale differences across datasets, we apply different grid subsampling sizes dl_0 and input sphere radii R_{in} : for STPLS3D, $dl_0 = 0.3m$, $R_{in} = 30m$; for DALES, $dl_0 = 0.2m$, $R_{in} = 15m$.

During the source pre-training stage, we employ the SGD optimizer with momentum (0.98), a gradient clipping norm of 100.0, and an initial learning rate of 1×10^{-2} with an exponential decay strategy (multiplying by 0.1 every 100 epochs). The model is trained for a total of 800 epochs. Batch sizes are set to 2 (STPLS3D) and 8 (DALES), with 400 steps per epoch.

In the source-free adaptation stage, we freeze all weights except for the BN affine parameters. The student model is updated using the SGD optimizer with a reduced learning rate of 1×10^{-3} for 3 adaptation epochs. The teacher model evolves via EMA with a momentum of $\alpha = 0.999$. For H3D, we set the number of steps per epoch to 50 with a batch size of 2; for the T3D dataset, the steps are set to 40 with a batch size of 8. Additionally, the core hyperparameters of our method are set as follows: For the H3D dataset, the ensemble size in the stochastic multi-augmented ensemble is set to $V = 4$, and the anchor selection ratio for class-balanced local prototype estimation is

set to $\rho = 0.8$. For the T3D dataset, we maintain $V = 4$, while the anchor selection ratio is set to $\rho = 0.7$.

4.3. Evaluation Metrics

To quantitatively assess the performance of our method and the baselines, we employ two standard metrics: mean Intersection-over-Union (mIoU) and Overall Accuracy (OA). Let K denote the total number of semantic classes. For each class $k \in \{1, \dots, K\}$, we calculate the number of True Positives (TP_k), False Positives (FP_k), and False Negatives (FN_k) based on the confusion matrix.

mIoU is the primary metric for this task, providing a balanced measure of segmentation quality across all semantic classes. The Intersection-over-Union (IoU_k) for class k is computed as the ratio of the intersection to the union between the ground-truth and the prediction:

$$IoU_k = \frac{TP_k}{TP_k + FP_k + FN_k} \quad (11)$$

The final mIoU is the macro-average of the IoU scores over all K classes:

$$mIoU = \frac{1}{K} \sum_{k=1}^K IoU_k \quad (12)$$

This metric is particularly crucial for geospatial scenes as it mitigates the influence of dominant classes and provides a fair assessment of performance on rare but critical object categories.

OA measures the global classification accuracy. It is calculated as the ratio of the total number of correctly classified points to the total number of points:

$$OA = \frac{\sum_{k=1}^K TP_k}{N} \quad (13)$$

where $\sum_{k=1}^K TP_k$ represents the total correct predictions across all categories. OA serves as a supplementary metric to reflect global consistency.

4.4. Experiment Results

To validate the effectiveness of our method, we compare it against several representative approaches:

Source-only: This baseline directly applies the model pre-trained on the source domain to the target domain for inference without any adaptation.

AdaBN [55]: This method replaces the Batch Normalization (BN) layer statistics (mean and variance) of the source model with those estimated from the target domain data during inference, achieving adaptation without updating any model parameters.

TENT [32]: This method leverages unlabeled target data during inference. By minimizing the entropy of model predictions, it updates only the BN layer statistics and affine parameters, adapting to the target domain distribution shift.

SHOT [38]: SHOT freezes the source classifier and fine-tunes only the feature extraction module. It incorporates the Information Maximization (IM) principle to encourage the model

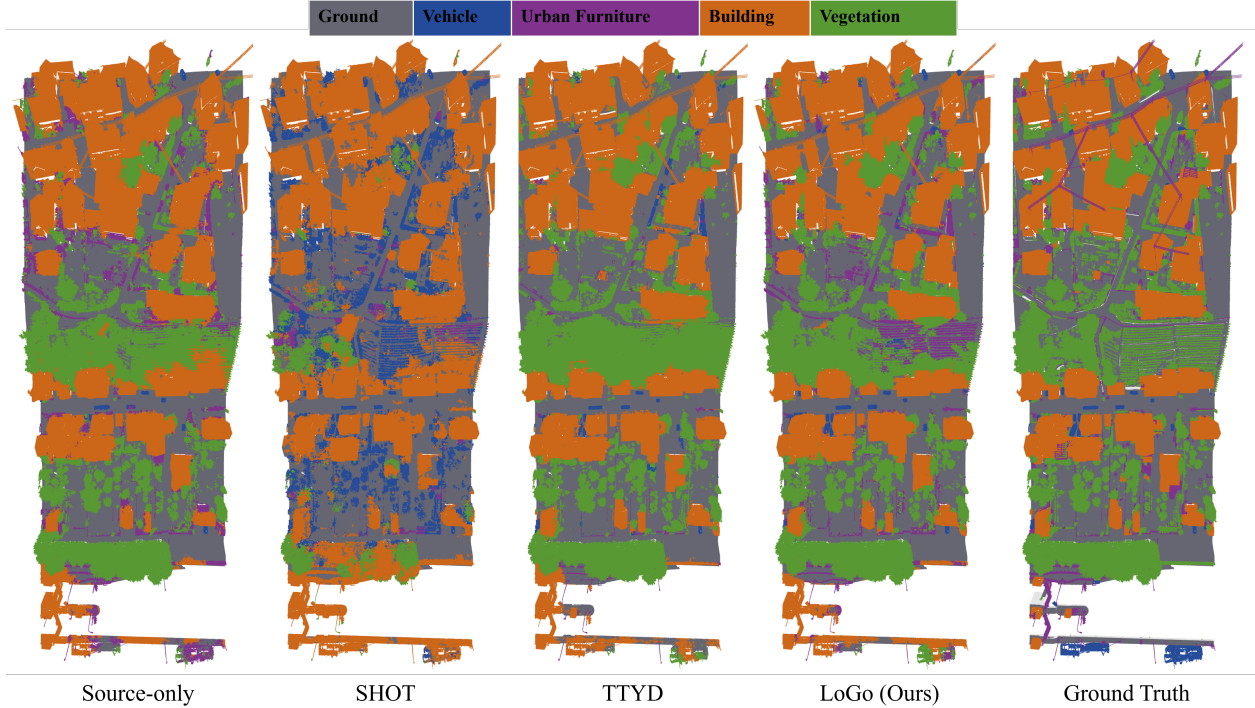


Figure 5: Qualitative comparison of global semantic segmentation results on the H3D dataset. From left to right: Source-only, SHOT, TTYD, LoGo, and Ground Truth.

to produce discriminative and globally diverse outputs. Furthermore, it employs a self-supervised pseudo-labeling strategy by computing class centroids within the target feature space to generate reliable pseudo-labels, thereby guiding feature alignment.

SHOT-ELR [56]: Addressing potential pseudo-label noise, this method builds upon SHOT by introducing a plug-and-play Early Learning Regularization (ELR) term. It utilizes the temporal moving average of historical predictions to guide current training, aiming to prevent overfitting to erroneous pseudo-labels.

TTYD [7]: This method fine-tunes the BN layers of the source model by minimizing prediction entropy and using source domain priors. It calculates prediction consistency between the current and a reference model (e.g., a PTBN model with adapted statistics only) to detect model degradation and trigger early stopping. This metric is also used for hyperparameter selection on the unlabeled target domain. An optimal model is then selected for pseudo-label generation in a second self-training stage.

Wang et al. [48]: This method fine-tunes only the BN layers of the pre-trained model. It employs a Progressive Batch Normalization (PBN) module to continuously incorporate test data statistics into the model. A self-supervised optimization strategy encourages high-confidence predictions through information maximization. Reliable pseudo-labels are generated by jointly evaluating entropy-based confidence and contrastive consistency.

4.4.1. Analysis on STPLS3D \rightarrow H3D

Table 1 details the transfer results from synthetic photogrammetric point clouds to real-world UAV LiDAR data. This cross-modality setting presents a challenging validation scenario due to the fundamental differences in imaging mechanisms (passive optical reconstruction and active laser scanning) and distinct noise patterns between the source and target domains.

The Source-only baseline exhibits poor generalization, achieving a low mIoU due to significant domain shift. While majority categories (e.g., Ground, Building) maintain reasonable performance, severe misclassification errors occur in categories like Vehicle and Urban Furniture. As shown in Fig. 5, Vehicle samples are frequently misclassified as Urban Furniture. Lightweight adaptation methods (AdaBN, TENT) achieve only marginal overall improvements. While they slightly improve the Vehicle category (reaching 28.17% and 23.96%, respectively), they suffer from performance degradation in tail classes. This suggests that solely minimizing prediction entropy on noisy target data exacerbates "confirmation bias," compelling the model to become over-confident in erroneous predictions while disregarding harder categories.

Notably, SHOT exhibits severe "negative transfer," with its mIoU dropping to 33.20% (a decrease of 15.63% compared to the Source-only baseline). Accuracy drops significantly in Vehicle, Urban Furniture, and Vegetation categories; as shown in Fig. 5, many samples are misidentified as Vehicle. We attribute this failure to the limitation of SHOT's greedy prototype assignment in cross-sensor scenarios. Since target features extracted by the source model are highly distorted, simple Euclidean distance-based matching leads to the "Winner-Takes-All" phe-

Table 1: **Quantitative comparison with state-of-the-art methods on the STPLS3D \rightarrow H3D transfer task.** The reported metrics include per-class IoU, mean IoU (mIoU), and Overall Accuracy (OA). The best results are highlighted in **bold**, and the second-best results are underlined.

Method	IoU					mIoU	OA
	Ground	Vehicle	Urban Fur.	Building	Vegetation		
Source-only	76.73	20.01	<u>12.22</u>	79.49	55.71	48.83	82.12
AdaBN [55]	77.69	28.17	10.01	80.02	54.46	50.07	82.86
TENT [32]	77.46	23.96	9.93	79.92	56.42	49.54	83.07
SHOT [38]	78.91	4.40	2.48	66.22	13.97	33.20	72.80
SHOT-ELR [56]	84.83	20.01	11.31	<u>86.33</u>	49.67	50.43	<u>84.67</u>
TTYD [7]	76.06	33.82	6.56	85.74	<u>56.45</u>	51.73	84.07
LoGo (Ours)	<u>81.47</u>	<u>30.84</u>	13.10	87.61	60.74	54.75	85.98

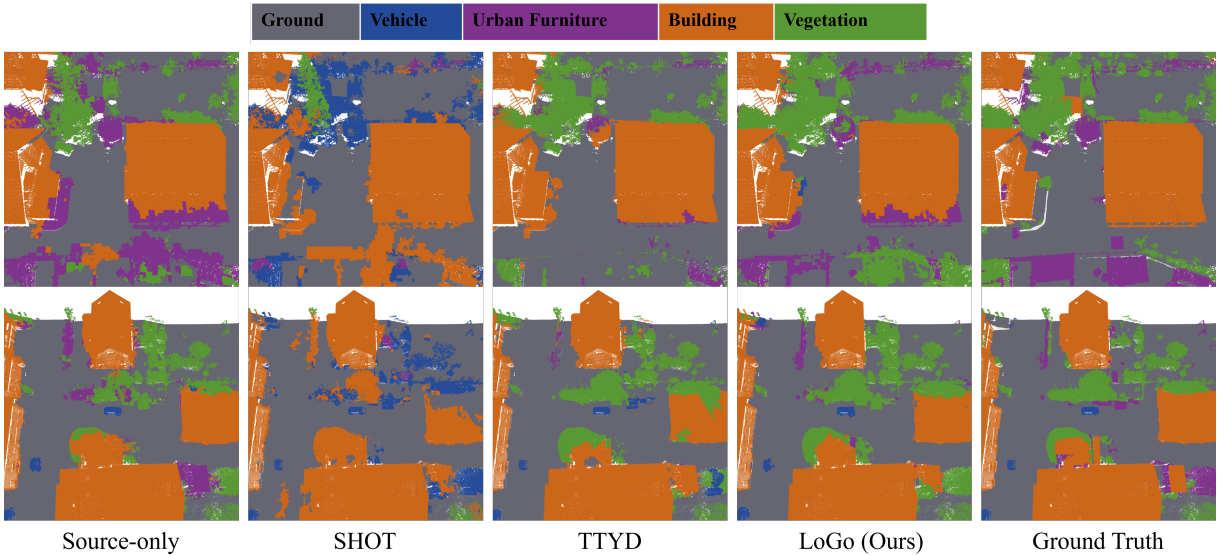


Figure 6: Qualitative comparison of local semantic segmentation details on the H3D dataset.

nomenon, where ambiguous samples are erroneously gravitate towards dominant class centroids. SHOT-ELR attempts to improve robustness by regularizing training with a moving average of historical predictions, but its improvement is limited. TTYD attempts adaptation through entropy minimization and source domain priors, but this can lead to accuracy degradation in small categories like Urban Furniture, misidentifying them as Building, as shown in Fig. 6.

In contrast, our approach achieves the best performance across all metrics (mIoU 54.75%, OA 85.98%), surpassing the Source-only baseline by 5.92% and avoiding the catastrophic failure seen in SHOT. This robustness stems from the synergy of our three mechanisms: First, mitigating the long-tailed distribution of geospatial data, the CBLPE module employs an intra-class independent mining strategy to ensure that reliable feature anchors are extracted even for sparse categories (e.g., Urban Furniture). Complementarily, the GDA module utilizes Optimal Transport to introduce global distribution constraints. This effectively rectifies the "Winner-Takes-All" bias inherent in greedy assignment strategies, preventing the severe negative transfer observed in SHOT and allowing samples with ambiguous semantic features (due to sensor discrepancies) to be

aligned with their respective categories based on global class priors. Ultimately, the LGDCF module establishes a rigorous filtering mechanism by mutually verifying local predictions against global assignments. This dual-consensus strategy filters out inconsistent pseudo-labels, ensuring that the student model is supervised only by high-confidence signals. Specifically, in the challenging Urban Furniture category, our IoU reaches 13.10%, substantially higher than that of TTYD; in the Vegetation category, we also maintain a high accuracy of 60.74%. These results demonstrate that in challenging scenarios with severe sensor heterogeneity, our method effectively mitigates domain shifts by enforcing a consensus between class-balanced local feature discrimination and global distributional alignment, thereby robustly rectifying biases induced by sensor heterogeneity.

4.4.2. Analysis on DALES \rightarrow Toronto-3D

Table 2 details the transfer results from the ALS dataset to the MLS dataset. This setting involves a significant viewpoint shift from a "high-altitude nadir view" to a "ground-level street view," leading to distinct performance among different adaptation mechanisms.

Table 2: **Quantitative comparison with different methods on the DALES \rightarrow T3D transfer task.** The reported metrics include per-class IoU, mean IoU (mIoU), and Overall Accuracy (OA). The best results are highlighted in **bold**, and the second-best results are underlined. Note that the results for Wang et al. [48] are cited directly from the original paper.

Method	IoU							mIoU	OA
	Road	Natural	Car	Utility line	Fence	Pole	Building		
Source-only	97.96	77.84	46.89	65.35	5.81	50.53	48.27	56.09	92.29
AdaBN [55]	97.42	67.06	12.50	51.34	7.27	15.57	31.35	40.36	88.82
TENT [32]	97.46	63.25	8.78	47.63	6.81	12.12	19.64	36.53	87.45
SHOT [38]	97.17	85.97	62.00	<u>65.80</u>	<u>16.40</u>	30.70	<u>71.14</u>	61.31	<u>94.34</u>
SHOT-ELR [56]	96.73	60.86	66.71	0.00	0.16	0.00	1.30	32.25	86.75
TTYD [7]	97.35	72.58	0.43	52.04	7.50	10.02	50.79	41.53	90.33
Wang et al. [48]	98.09	<u>86.99</u>	<u>72.72</u>	60.12	3.07	<u>60.34</u>	53.50	<u>62.12</u>	92.67
LoGo (Ours)	97.85	92.30	83.50	72.95	21.13	62.59	84.46	73.54	96.93

AdaBN replaces BN statistics with local means of the target domain, leading to a drop in mIoU to 40.36%. This failure is attributed to the spatially non-uniform scanning characteristics of MLS data, which result in statistics that deviate significantly from the global distribution. Normalizing features with these biased local statistics compromises the model’s original decision boundaries. TENT further exacerbates this decline to 36.53%; its strategy of minimization of local batch entropy leads to overfitting dominant classes (e.g., Road) within extremely unbalanced data streams, triggering the forgetting of sparse categories (e.g., Fence).

SHOT utilizes global prototype estimation to mitigate local noise, raising mIoU to 61.31%. However, its distance-based greedy matching can cause misclassifications, such as Pole being misclassified as Building (Fig. 8). In contrast, SHOT-ELR suffers a performance drop (mIoU 32.25%) because its ELR mechanism proves overly conservative. It erroneously identifies key geometric features distorted by viewpoint shifts (e.g.,

Utility line) as label noise and suppresses them, hindering the model’s ability to learn hard samples. TTYD is severely limited by "Label Distribution Shift." By forcing the prediction distribution of MLS data to align with the discrepant ALS prior, it causes the target-specific dominant category (e.g., Car) to be erroneously under-represented, with accuracy dropping to 0.43% (Fig. 7).

Additionally, the method of Wang et al. achieves the best result on the Road category (98.09%), benefiting from its progressive BN update strategy’s ability to smoothly adapt to spatially dominant categories with stable feature statistics. However, its failure on Fence (3.07%) again exposes the shortcoming of online TTA: when facing long-tailed distributions, the scarcity of rare categories in local batches prevents the accumulation of sufficient gradients, ultimately leading to the "Winner-Takes-All" effect.

In contrast, our method achieves a mIoU of 73.54%, demonstrating superior robustness across all metrics. This success

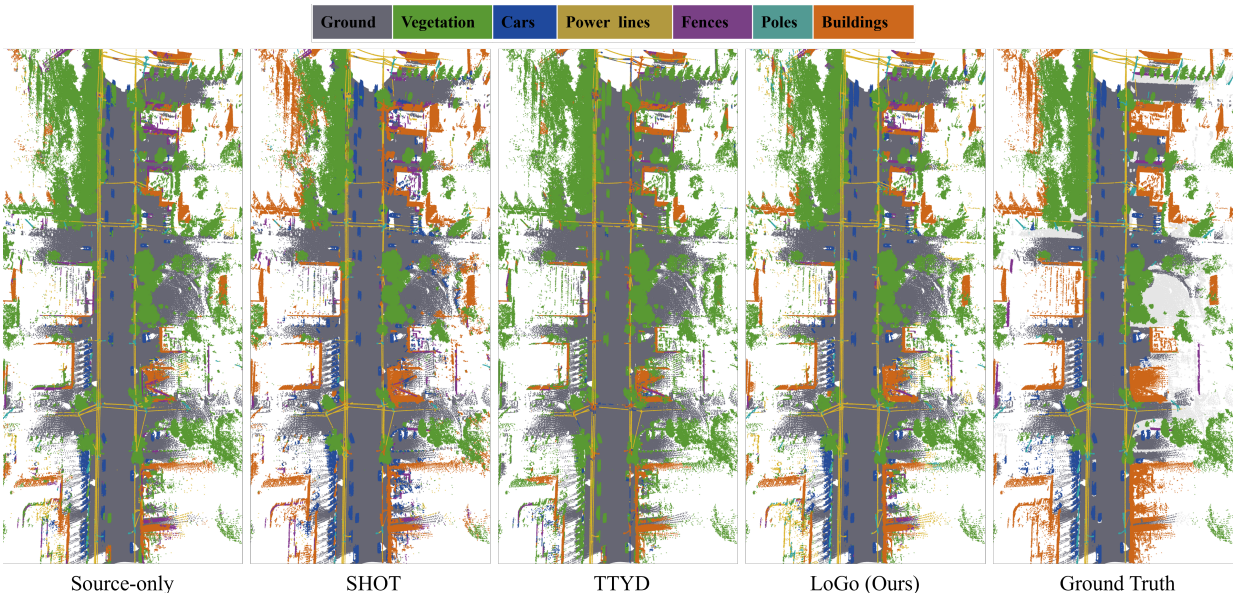


Figure 7: Qualitative comparison of global semantic segmentation results on the T3D dataset. From left to right: Source-only, SHOT, TTYD, LoGo, and Ground Truth.

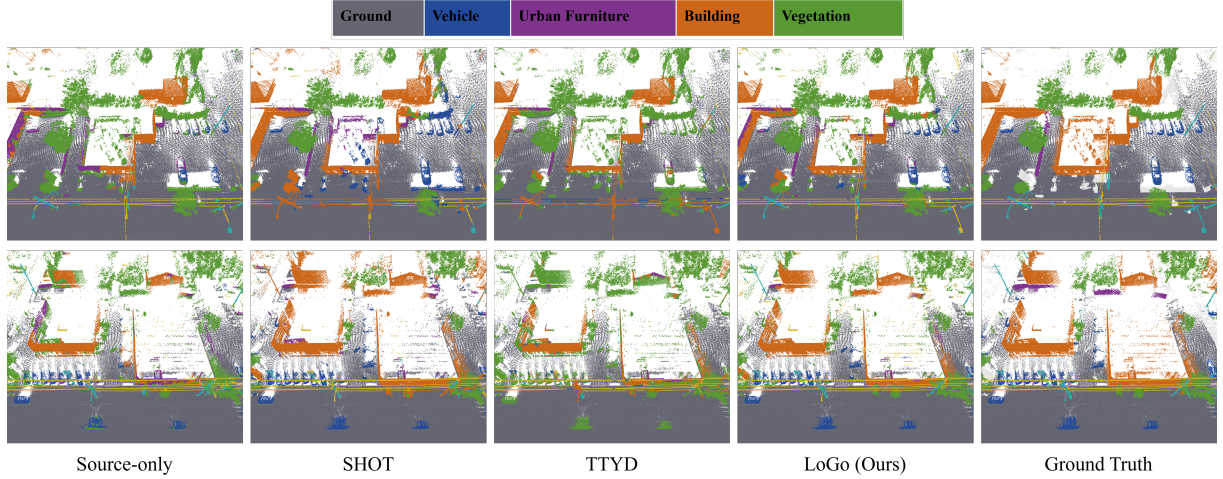


Figure 8: Qualitative comparison of local semantic segmentation details on the T3D dataset.

stems from the synergy of three mechanisms. First, the CBLPE module adopts an "intra-class independent mining" strategy. By prioritizing relative ranking within categories, it preserves feature anchors for sparse classes like Fence, thereby alleviating forgetting and raising its IoU to 21.13%. Second, the GDA module introduces global distribution constraints via Optimal Transport. This mechanism rectifies the "Winner-Takes-All" bias inherent in SHOT's greedy strategy, while simultaneously avoiding the mismatched label distribution constraints imposed by TTYD's source priors. By aligning samples based on dynamically estimated target priors, GDA ensures structurally consistent predictions for geometric objects like Utility lines and Poles. Finally, the LGDCF module rigorously filters samples through a "local-global" dual verification mechanism. This effectively mitigates the propagation of pseudo-label noise, preventing the accumulation of erroneous supervision signals and enhancing adaptation stability in complex scenes.

4.5. Experimental Analysis

4.5.1. Ablation Study

Ablation Setup. To evaluate the efficacy of each module, we compare the Source-only baseline with three variants of our framework: (1) CBLPE-only: This variant employs a standard prototype-based pseudo-labeling strategy. Without global constraints, pseudo-labels are generated via a greedy assignment strategy, mapping each sample to its nearest class prototype based solely on feature similarity. (2) CBLPE+GDA: This variant introduces global distribution alignment. Instead of local matching, pseudo-labels are derived directly from the global assignment plan computed by the Optimal Transport mechanism, enforcing distribution-level constraints. (3) LoGo (Full Method): This setting activates the complete Local-Global Dual-Consensus Filtering. Here, the final supervision signal is determined by taking the intersection of the initial ensemble predictions and the global transport assignments, retaining only those samples where both perspectives reach a consensus.

Analysis. As shown in Table 3, the ablation results underscore the necessity of our holistic Local-Global frame-

Table 3: **Ablation study of the proposed framework on STPLS3D → H3D and DALES → T3D.** The best results are highlighted in **bold**.

Module			STPLS3D → H3D		DALES → T3D	
CBLPE	GDA	LGDCF	mIoU	OA	mIoU	OA
			48.83	82.12	56.09	92.29
✓			45.60	74.63	58.33	92.25
✓	✓		52.75	85.02	66.14	95.19
✓	✓	✓	54.75	85.98	73.54	96.93

work. The Source-only baseline (Row 1) shows limited performance due to significant domain shift. Notably, when enabling CBLPE-only (Row 2), we observe a performance degradation on the STPLS3D dataset (48.83% → 45.60%). This suggests that naive greedy assignment based on potentially noisy prototypes exacerbates confirmation bias, where initial misclassifications are reinforced during self-training. However, the integration of GDA (Row 3) reverses this trend, leading to substantial improvement over the baseline on both datasets. This demonstrates that introducing global distribution constraints and inter-class competition effectively rectifies the assignment biases inherent in the local view. Ultimately, the Full Method (Row 4) achieves the optimal performance by enforcing the dual-consensus mechanism. By rigorously filtering out ambiguous boundary samples where the local and global views conflict, this strategy yields reliable pseudo-labels, effectively mitigating noise propagation as evidenced by the superior 73.54% mIoU on the DALES dataset.

4.5.2. Parameter Sensitivity Analysis

To evaluate the robustness of our proposed framework and the influence of key hyperparameters, we conduct a detailed sensitivity analysis on the STPLS3D → H3D and DALES → T3D benchmarks. We focus on two core parameters: the *Ensemble Size* (V) used in the multi-augmented inference, and the *Anchor Selection Ratio* (ρ) used in the class-balanced local prototype estimation. The quantitative results are illustrated in Figure 9.

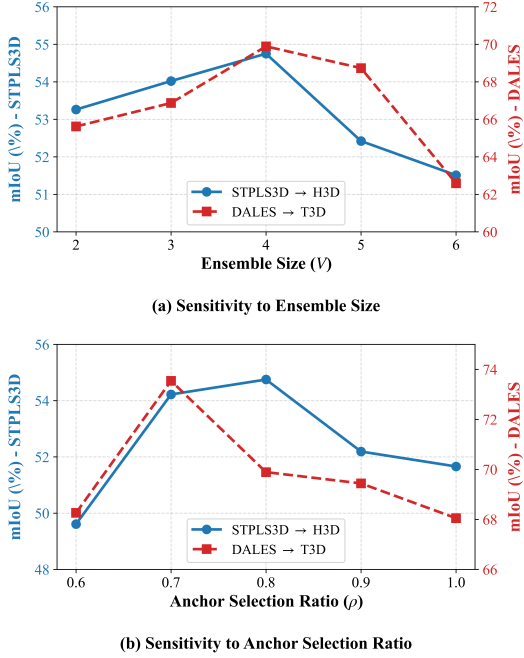


Figure 9: Parameter sensitivity analysis on STPLS3D → H3D and DALES → T3D tasks. (a) Impact of the ensemble size V on segmentation performance; (b) Impact of the anchor selection ratio ρ on local prototype estimation.

Impact of Ensemble Size V . As shown in Figure 9 (a), segmentation performance increases initially before decreasing as V grows. We observe a significant improvement in mIoU on both datasets when V increases from 2 to 4. This indicates that a moderate ensemble size effectively exploits the prediction consistency across different geometric transformations, thereby smoothing out prediction variance during inference. However, when V exceeds 4 (e.g., $V = 6$), the performance suffers a slight decline. We attribute this to the fact that excessive stochastic augmentations might introduce distortions, causing predictions in certain views to deviate from the true distribution and degrading the quality of pseudo-labels. Consequently, we adopt $V = 4$ as the optimal trade-off between adaptation accuracy and computational cost.

Impact of Anchor Selection Ratio ρ . The parameter ρ determines the proportion of high-confidence samples retained for calculating class prototypes. As depicted in Figure 9 (b), the model performance is sensitive to ρ . The mIoU peaks at $\rho = 0.8$ for STPLS3D and $\rho = 0.7$ for DALES. This underscores the critical trade-off between *representativeness* and *noise robustness*. Selecting the top 70%-80% of samples ensures that the computed prototypes are sufficiently representative of the intra-class distribution while effectively filtering out ambiguous samples near decision boundaries. Notably, setting $\rho = 1.0$ (i.e., using all predicted samples) leads to a performance drop, confirming the necessity of our Top-K anchor mining strategy in preventing prototype contamination by noisy pseudo-labels.

5. Conclusion

In this paper, we address the challenging problem of source-free unsupervised domain adaptation for semantic segmentation of heterogeneous geospatial point clouds under privacy and regulatory constraints. To this end, we propose LoGo, a self-training framework that effectively mitigates severe cross-scene and cross-sensor domain shifts without access to source data. Extensive experiments on challenging cross-domain benchmarks demonstrate consistent and significant performance gains. These results establish SFUDA as a crucial and feasible paradigm for large-scale geospatial point cloud semantic segmentation in real-world surveying and remote sensing scenarios, and demonstrate that robust adaptation critically depends on the synergy between local class-balanced feature discrimination and global distributional alignment when learning from unlabeled and long-tailed point clouds. Future work will focus on improving the robustness of domain adaptation under more extreme label distribution shifts, and extending the SFUDA framework to handle target scenes with missing or unseen categories.

Acknowledgements

This work was supported by the National Natural Science Foundation of China under Grant 62575039 and 42271365.

References

- [1] S. Xia, S. Xu, R. Wang, J. Li, G. Wang, Building instance mapping from als point clouds aided by polygonal maps, *IEEE Transactions on Geoscience and Remote Sensing* 60 (2021) 1–13.
- [2] Y. Gao, S. Xia, C. Wang, X. Xi, B. Yang, C. Xie, Semantic segmentation of airborne lidar point clouds with noisy labels, *IEEE Transactions on Geoscience and Remote Sensing* 62 (2024) 1–14.
- [3] J. Shao, W. Yao, P. Wang, Z. He, L. Luo, Urban geobim construction by integrating semantic lidar point clouds with as-designed bim models, *IEEE Transactions on Geoscience and Remote Sensing* 62 (2024) 1–12.
- [4] C. R. Qi, L. Yi, H. Su, L. J. Guibas, Pointnet++: deep hierarchical feature learning on point sets in a metric space, in: *Proceedings of the 31st International Conference on Neural Information Processing Systems*, Curran Associates Inc., 2017, p. 5105–5114.
- [5] H. Thomas, C. R. Qi, J.-E. Deschaud, B. Marcotegui, F. Goulette, L. J. Guibas, Kpconv: Flexible and deformable convolution for point clouds, in: *Proceedings of the IEEE/CVF international conference on computer vision*, 2019, pp. 6411–6420.

[6] H. Luo, K. Khoshelham, L. Fang, C. Chen, Unsupervised scene adaptation for semantic segmentation of urban mobile laser scanning point clouds, *ISPRS Journal of Photogrammetry and Remote Sensing* 169 (2020) 253–267.

[7] B. Michele, A. Boulch, T.-H. Vu, G. Puy, R. Marlet, N. Courty, Train till you drop: Towards stable and robust source-free unsupervised 3d domain adaptation, in: *European Conference on Computer Vision*, Springer, 2024, pp. 1–19.

[8] N. Varney, V. K. Asari, Q. Graehling, Dales: A large-scale aerial lidar data set for semantic segmentation, in: *Proceedings of the IEEE/CVF conference on computer vision and pattern recognition workshops*, 2020, pp. 186–187.

[9] F. J. Lawin, M. Danelljan, P. Tostberg, G. Bhat, F. S. Khan, M. Felsberg, Deep projective 3d semantic segmentation, in: *International conference on computer analysis of images and patterns*, Springer, 2017, pp. 95–107.

[10] A. Boulch, B. L. Saux, N. Audebert, Unstructured point cloud semantic labeling using deep segmentation networks, in: *Proceedings of the Workshop on 3D Object Retrieval*, Eurographics Association, 2017, p. 17–24.

[11] B. Graham, M. Engelcke, L. Van Der Maaten, 3d semantic segmentation with submanifold sparse convolutional networks, in: *Proceedings of the IEEE conference on computer vision and pattern recognition*, 2018, pp. 9224–9232.

[12] C. Choy, J. Gwak, S. Savarese, 4d spatio-temporal convnets: Minkowski convolutional neural networks, in: *Proceedings of the IEEE/CVF conference on computer vision and pattern recognition*, 2019, pp. 3075–3084.

[13] Y. Wang, Y. Sun, Z. Liu, S. E. Sarma, M. M. Bronstein, J. M. Solomon, Dynamic graph cnn for learning on point clouds, *ACM Trans. Graph.* 38 (2019).

[14] Q. Hu, B. Yang, L. Xie, S. Rosa, Y. Guo, Z. Wang, N. Trigoni, A. Markham, Randla-net: Efficient semantic segmentation of large-scale point clouds, in: *Proceedings of the IEEE/CVF conference on computer vision and pattern recognition*, 2020, pp. 11108–11117.

[15] H. Zhao, L. Jiang, J. Jia, P. H. Torr, V. Koltun, Point transformer, in: *Proceedings of the IEEE/CVF international conference on computer vision*, 2021, pp. 16259–16268.

[16] X. Wu, L. Jiang, P.-S. Wang, Z. Liu, X. Liu, Y. Qiao, W. Ouyang, T. He, H. Zhao, Point transformer v3: Simpler faster stronger, in: *Proceedings of the IEEE/CVF conference on computer vision and pattern recognition*, 2024, pp. 4840–4851.

[17] S. Zhao, Y. Wang, B. Li, B. Wu, Y. Gao, P. Xu, T. Darrell, K. Keutzer, epointda: An end-to-end simulation-to-real domain adaptation framework for lidar point cloud segmentation, in: *Proceedings of the AAAI Conference on Artificial Intelligence*, volume 35, 2021, pp. 3500–3509.

[18] L. Yi, B. Gong, T. Funkhouser, Complete & label: A domain adaptation approach to semantic segmentation of lidar point clouds, in: *Proceedings of the IEEE/CVF conference on computer vision and pattern recognition*, 2021, pp. 15363–15373.

[19] A. Xiao, J. Huang, D. Guan, F. Zhan, S. Lu, Transfer learning from synthetic to real lidar point cloud for semantic segmentation, in: *Proceedings of the AAAI conference on artificial intelligence*, volume 36, 2022, pp. 2795–2803.

[20] G. Li, G. Kang, X. Wang, Y. Wei, Y. Yang, Adversarially masking synthetic to mimic real: Adaptive noise injection for point cloud segmentation adaptation, in: *Proceedings of the IEEE/CVF Conference on Computer Vision and Pattern Recognition*, 2023, pp. 20464–20474.

[21] Z. Yuan, M. Cheng, W. Zeng, Y. Su, W. Liu, S. Yu, C. Wang, Prototype-guided multitask adversarial network for cross-domain lidar point clouds semantic segmentation, *IEEE Transactions on Geoscience and Remote Sensing* 61 (2023) 1–13.

[22] L. Kong, N. Quader, V. E. Liong, Conda: Unsupervised domain adaptation for lidar segmentation via regularized domain concatenation, *2023 IEEE International Conference on Robotics and Automation (ICRA)* (2021) 9338–9345.

[23] C. Saltori, F. Galasso, G. Fiameni, N. Sebe, E. Ricci, F. Poiesi, Cosmix: Compositional semantic mix for domain adaptation in 3d lidar segmentation, in: *European conference on computer vision*, Springer, 2022, pp. 586–602.

[24] A. Xiao, J. Huang, D. Guan, K. Cui, S. Lu, L. Shao, Polarmix: A general data augmentation technique for lidar point clouds, *Advances in Neural Information Processing Systems* 35 (2022) 11035–11048.

[25] A. Shaban, J. Lee, S. Jung, X. Meng, B. Boots, Lidaruda: Self-ensembling through time for unsupervised lidar domain adaptation, in: *Proceedings of the IEEE/CVF International Conference on Computer Vision*, 2023, pp. 19784–19794.

[26] H. Luo, Z. Chen, F. Ye, T. Huang, H. He, W. Hu, Cross-sensor adaptive semantic segmentation for mobile laser scanning point clouds based on continuous potential scene surface reconstruction, *ISPRS Journal of Photogrammetry and Remote Sensing* 228 (2025) 537–551.

[27] J. N. Kundu, N. Venkat, R. V. Babu, et al., Universal source-free domain adaptation, in: *Proceedings of the IEEE/CVF conference on computer vision and pattern recognition*, 2020, pp. 4544–4553.

[28] V. K. Kurmi, V. K. Subramanian, V. P. Namboodiri, Domain impression: A source data free domain adaptation

method, in: Proceedings of the IEEE/CVF winter conference on applications of computer vision, 2021, pp. 615–625.

[29] Z. Qiu, Y. Zhang, H. Lin, S. Niu, Y. Liu, Q. Du, M. Tan, Source-free domain adaptation via avatar prototype generation and adaptation, in: Z.-H. Zhou (Ed.), Proceedings of the Thirtieth International Joint Conference on Artificial Intelligence, IJCAI-21, International Joint Conferences on Artificial Intelligence Organization, 2021, pp. 2921–2927. Main Track.

[30] R. Li, Q. Jiao, W. Cao, H.-S. Wong, S. Wu, Model adaptation: Unsupervised domain adaptation without source data, in: 2020 IEEE/CVF Conference on Computer Vision and Pattern Recognition (CVPR), 2020, pp. 9638–9647.

[31] Y. Liu, W. Zhang, J. Wang, Source-free domain adaptation for semantic segmentation, in: 2021 IEEE/CVF Conference on Computer Vision and Pattern Recognition (CVPR), 2021, pp. 1215–1224.

[32] D. Wang, E. Shelhamer, S. Liu, B. Olshausen, T. Darrell, Tent: Fully test-time adaptation by entropy minimization, in: International Conference on Learning Representations, 2021.

[33] M. J. Mirza, J. Micorek, H. Possegger, H. Bischof, The norm must go on: Dynamic unsupervised domain adaptation by normalization, in: Proceedings of the IEEE/CVF conference on computer vision and pattern recognition, 2022, pp. 14765–14775.

[34] S. Yang, Y. Wang, J. Van De Weijer, L. Herranz, S. Jui, Generalized source-free domain adaptation, in: Proceedings of the IEEE/CVF international conference on computer vision, 2021, pp. 8978–8987.

[35] S. Yang, S. Jui, J. Van De Weijer, et al., Attracting and dispersing: A simple approach for source-free domain adaptation, *Advances in Neural Information Processing Systems* 35 (2022) 5802–5815.

[36] K. Tanwisuth, X. Fan, H. Zheng, S. Zhang, H. Zhang, B. Chen, M. Zhou, A prototype-oriented framework for unsupervised domain adaptation, *Advances in Neural Information Processing Systems* 34 (2021) 17194–17208.

[37] N. Karim, N. C. Mithun, A. Rajvanshi, H.-p. Chiu, S. Samarasekera, N. Rahnavard, C-sfda: A curriculum learning aided self-training framework for efficient source free domain adaptation, in: Proceedings of the IEEE/CVF conference on computer vision and pattern recognition, 2023, pp. 24120–24131.

[38] J. Liang, D. Hu, J. Feng, Do we really need to access the source data? source hypothesis transfer for unsupervised domain adaptation, in: International conference on machine learning, PMLR, 2020, pp. 6028–6039.

[39] J. Duan, Y. Zhang, Y. Qu, Source-free domain adaptation for point cloud semantic segmentation, in: 2024 IEEE International Conference on Multimedia and Expo (ICME), IEEE, 2024, pp. 1–6.

[40] C. Saltori, S. Lathuilière, N. Sebe, E. Ricci, F. Galasso, Sf-uda 3d: Source-free unsupervised domain adaptation for lidar-based 3d object detection, in: 2020 International Conference on 3D Vision (3DV), IEEE, 2020, pp. 771–780.

[41] D. Hegde, V. Kilic, V. Sindagi, A. B. Cooper, M. Foster, V. M. Patel, Source-free unsupervised domain adaptation for 3d object detection in adverse weather, in: 2023 IEEE International Conference on Robotics and Automation (ICRA), IEEE, 2023, pp. 6973–6980.

[42] D. Tsai, J. S. Berrio, M. Shan, E. Nebot, S. Worrall, Ms3d++: Ensemble of experts for multi-source unsupervised domain adaptation in 3d object detection, *IEEE Transactions on Intelligent Vehicles* 10 (2025) 1999–2014.

[43] Z. Xia, H. Xia, S. Jin, W. Wang, Z. Ding, X. Cao, Dspf: Dual-stage preservation and fusion for source-free domain adaptive point cloud completion, in: Proceedings of the 33rd ACM International Conference on Multimedia, 2025, pp. 8428–8437.

[44] X. He, Z. Zhu, L. Nan, H. Chen, J. Qin, M. Wei, Pointsfda: Source-free domain adaptation for point cloud completion, *arXiv preprint arXiv:2503.15144* (2025).

[45] S. Wang, Y. Tong, X. Shang, Z. Zhang, Multi-confidence guided source-free domain adaption method for point cloud primitive segmentation, in: 2024 IEEE International Conference on Robotics and Automation (ICRA), IEEE, 2024, pp. 737–743.

[46] S. Wang, Y. Tong, R. Xu, Z. Zhang, Sdaps*: A novel source-free domain adaption method for point cloud primitive segmentation, *IEEE Transactions on Industrial Informatics* 22 (2026) 14–25.

[47] Y. Liu, H. Zhu, Y. Lei, H. Liu, Y. Pei, Y. Guo, Sf-city: A source-free domain adaptation method for city-scale point cloud semantic segmentation, *IEEE Transactions on Multimedia* 27 (2025) 6908–6921.

[48] P. Wang, W. Yao, J. Shao, Z. He, Test-time adaptation for geospatial point cloud semantic segmentation with distinct domain shifts, *ISPRS Journal of Photogrammetry and Remote Sensing* 229 (2025) 422–435.

[49] A. Tarvainen, H. Valpola, Mean teachers are better role models: Weight-averaged consistency targets improve semi-supervised deep learning results, *Advances in neural information processing systems* 30 (2017).

[50] C. Villani, et al., *Optimal transport: old and new*, volume 338, Springer, 2008.

- [51] R. Sinkhorn, Diagonal equivalence to matrices with prescribed row and column sums, *The American Mathematical Monthly* 74 (1967) 402–405.
- [52] M. Chen, Q. Hu, Z. Yu, H. THOMAS, A. Feng, Y. Hou, K. McCullough, F. Ren, L. Soibelman, Stpls3d: A large-scale synthetic and real aerial photogrammetry 3d point cloud dataset, in: 33rd British Machine Vision Conference 2022, BMVC 2022, London, UK, November 21-24, 2022, BMVA Press, 2022.
- [53] M. Kölle, D. Laupheimer, S. Schmohl, N. Haala, F. Rottensteiner, J. D. Wegner, H. Ledoux, The hessigheim 3d (h3d) benchmark on semantic segmentation of high-resolution 3d point clouds and textured meshes from uav lidar and multi-view-stereo, *ISPRS Open Journal of Photogrammetry and Remote Sensing* 1 (2021) 100001.
- [54] W. Tan, N. Qin, L. Ma, Y. Li, J. Du, G. Cai, K. Yang, J. Li, Toronto-3d: A large-scale mobile lidar dataset for semantic segmentation of urban roadways, in: Proceedings of the IEEE/CVF conference on computer vision and pattern recognition workshops, 2020, pp. 202–203.
- [55] Y. Li, N. Wang, J. Shi, J. Liu, X. Hou, Revisiting batch normalization for practical domain adaptation, *arXiv preprint arXiv:1603.04779* (2016).
- [56] L. Yi, G. Xu, P. Xu, J. Li, R. Pu, C. Ling, I. McLeod, B. Wang, When source-free domain adaptation meets learning with noisy labels, in: The Eleventh International Conference on Learning Representations, 2023.